Sediment transport in combined wave-current seabed boundary layers due to streaming

Mohammad Saud Afzal[1]; Lars Erik Holmedal[2]; and Dag Myrhaug[3]

Abstract: The effect of wave-induced streaming on the seabed boundary layer sediment transport (i.e. bedload and suspended sediment transport) has been investigated for following and opposing waves and current where the wave propagation forms a nonzero angle with the current. The mean sediment transport results from an interaction between Longuet-Higgins streaming, streaming due to wave skewness and wave-current interaction. For collinear waves the mean sediment transport is directed along the wave propagation direction with the largest transport taking place beneath following waves and current. ~~It appears that t~~The mean sediment transport decreases as the angle between the waves and the current increases. For a given angle, the sediment transport is largest for second order Stokes waves, followed by linear propagating waves, horizontally uniform Stokes forcing and horizontally uniform linear forcing. The mean sediment transport direction is rotated from the wave propagation direction towards the current and this rotation is largest for horizontally uniform linear forcing, followed by horizontally uniform Stokes forcing, linear propagating waves and second order Stokes waves.

Author keywords: Hydraulics; Sediment entrainment; Turbulent flow; Hydrodynamic force.

[1]Asst. Professor, Indian Institute of Technology, Kharagpur, India, (corresponding author). Email: saud@civil.iitkgp.ac.in

[2]Professor, Department of Marine Technology, Norwegian University of Science and Technology, Trondheim, Norway, Email: lars.erik.holmedal@ntnu.no

[3]Professor, Department of Marine Technology, Norwegian University of Science and Technology, Trondheim, Norway, Email: dag.myrhaug@ntnu.no

INTRODUCTION

In seabed boundary layers beneath propagating waves, a small vertical wave-induced near-bed velocity exists that gives rise to a weak mass transport. This happens because of the bottom friction leading to the horizontal and vertical velocity components not being 90° out of phase (as they are for potential flow), which again leads to the wave-averaged convective term (which contains the product of these velocity components) acting as a depth-varying force pushing the flow in the wave propagation direction. This is commonly referred to as Longuet-Higgins sea bed boundary layer streaming Longuet-Higgins (1953), which has been investigated in previous works **by e.g. (Afzal et al. 2015; Fuhrman et al. 2013; Holmedal et al. 2013; Holmedal and Myrhaug 2009; Kranenburg et al. 2012)**. Another kind of streaming, caused by turbulence asymmetry in successive wave half-cycles beneath skewed waves, is here referred to as streaming due to wave skewness. This streaming mechanism forces the flow against the wave direction and is thus representing a competing mechanism to the Longuet-Higgins streaming for second order Stokes waves as investigated in detail in Holmedal and Myrhaug (2009). Measurements of streaming due to wave skewness in oscillatory water tunnels were first reported by Ribberink and Al-Salem (1995) for waves alone, and by Yuan and Madsen (2015) for following and opposing waves and current. The rough bed measurements by Ribberink and Al-Salem (1995) were well predicted by Davies and Li (1997) and Holmedal and Myrhaug (2006) (using $k-1$ and $k-\in$ turbulence closure models, respectively), while Scandura (2007) investigated streaming due to wave skewness over a smooth bed resolving the turbulent flow by direct numerical simulations. The predictions by Afzal et al. (2015) of streaming due to wave skewness in combined wave-current flows were in excellent agreement with the measurements by Yuan and Madsen (2015), showing that the effect of streaming due to wave skewness is to enhance and reduce the wave-averaged velocity when the waves are opposing and following the current, respectively. Similar qualitative results were predicted earlier by Holmedal et al. (2013) where the effect of streaming on the wave-current sea bed boundary layer for following and opposing waves plus current was investigated using numerical simulations.

Nielsen and Callaghan (2003) predicted the streaming-induced sediment transport for sheet flow conditions under waves alone using empirical formulas. These predictions were in good agreement with observations of Ribberink et al. (2000). More recently, the sediment transport

beneath a group of skewed waves was investigated by Yu et al. (2010) using a two-phase model (originally developed by Hsu et al. (2004)) that takes both the Longuet-Higgins and streaming due to wave skewness into account. Yu et al. (2010) found that the non-linearity of the waves accounted for most of the sediment transport for very skewed waves, whereas the sediment transport beneath less skewed waves is mainly due to Longuet-Higgins streaming. Furthermore, the sediment transport is always in the wave propagation direction, which is similar to the findings by Holmedal and Myrhaug (2009). Fuhrman et al. (2009) investigated the sediment transport beneath horizontally uniform second order Stokes boundary layer forcing over a flat bed and found that the sediment transport increased with increasing wave skewness which is consistent with the findings of Holmedal and Myrhaug (2006). Ruessink et al. (2009, 2011) and van der A et al. (2011) have presented further results on predicted and measured sediment transport beneath horizontally uniform second order Stokes forcing including the effect of wave skewness. Fuhrman et al. (2013) found that the Longuet-Higgins streaming and other convective effect promotes onshore sediment transport even for fine sand and highly skewed waves. Schretlen et al. (2011) found a larger onshore sediment transport for measurements conducted in a large wave flume (using second order Stokes waves) than for measurements conducted in oscillating water tunnels (using horizontally uniform Stokes forcing) where Longuet-Higgins streaming is absent. Similar results were also found by both Fuhrman et al. (2013) and Kranenburg et al. (2013) using numerical simulations. Some other important works on seabed boundary layers include, but not limited to are from Lee and Cheung (1999), Bose and Dey (2014) and Ali and Dey (2016).

Holmedal and Myrhaug (2009) found that the Longuet-Higgins streaming is the dominating mechanism providing wave-averaged (mean) sediment transport beneath waves alone over a flat bed. It appears that for median and coarse sand, the mean suspended sediment transport is of the same magnitude as the mean bedload transport whereas the total sediment transport for fine sediments is dominated by suspension. More recently, Afzal et al. (2015) investigated the effect of streaming on the wave-current sea bed boundary layer for waves with an angle of attack on the current using numerical simulations (k- $\in$ turbulence model). They studied the interaction between the classical wave-current interaction mechanism and the two competing streaming mechanisms which also affect the direction and veering of the resulting current; these effects cannot be measured neither in closed channels nor in large wave flumes.

In conclusion, the studies done earlier were limited to streaming and corresponding sediment transport either under waves or under collinear waves and current. However, the realistic situation in nature is that of waves propagating at an angle to the current. The aim of the present work is to investigate how wave-induced streaming, non-linear wave-forcing, wave-current interaction and sediment particle size affect the near-bed sediment dynamics and transport using numerical simulations. These numerical simulations are conducted for situations where the flow is considered to be wave-dominated including the situation where the waves propagate with a non-zero angle relative to the current. First the present sediment transport model is validated against laboratory measurements (bedload and suspended load) conducted in both an oscillating water tunnel (Dohmen-Janssen et al. 2001) and beneath propagating waves in a large scale flume (Dohmen-Janssen and Hanes 2002). Then numerical simulations are applied to investigate the sediment dynamics and transport beneath waves alone and beneath combined waves and current, for those sediments that the model has been validated against. This includes the sediment transport beneath combined waves and current, where wave propagation is in a different direction than the current direction, including following and opposing waves and current. To the best of authors' knowledge present work is the first study that investigates sediment transport in combined wave-current seabed boundary layers due to streaming. Despite the present lack of experimental data for these situations, the present work aim to yield new insight into the detailed bottom boundary layer sediment dynamics and transport.

NUMERICAL MODEL

Boundary layer flow near the ~~ocean bed~~seabed is considered over an infinitely long flat bottom fixed at $z = z_0 = k_N/30$ (Dey 2014), where k_N is the equivalent Nikuradse roughness. The horizontal coordinate x is taken in the free stream current direction, the horizontal direction perpendicular to the free stream current is represented by the coordinate y, and z denotes the vertical coordinate. Waves propagate at an angle θ relative to the current in the horizontal plane as given in ~~Afzal et al. (2015,~~ Fig. 1~~)~~. The hydrodynamic part of the model used in the study is the same as that presented in Afzal et al. (2015) and thus a brief description of the hydrodynamic model is given below along with sediment transport formulation.

Governing equations

The Reynolds-averaged boundary layer equations are given by

$$\frac{\partial u}{\partial t}+u\frac{\partial u}{\partial x}+v\frac{\partial u}{\partial y}+w\frac{\partial u}{\partial z}=-\frac{1}{\rho}\frac{\partial p}{\partial x}+\frac{\partial}{\partial z}\left(\nu_T\frac{\partial u}{\partial z}\right) \quad (11)$$

$$\frac{\partial v}{\partial t}+u\frac{\partial v}{\partial x}+v\frac{\partial v}{\partial y}+w\frac{\partial v}{\partial z}=-\frac{1}{\rho}\frac{\partial p}{\partial x}+\frac{\partial}{\partial z}\left(\nu_T\frac{\partial v}{\partial z}\right) \quad (22)$$

$$\frac{\partial u}{\partial x}+\frac{\partial v}{\partial y}+\frac{\partial w}{\partial z}=0 \quad (33)$$

where u, v and w are the velocity components in x, y and z direction respectively. Here, ρ is the density of water, p is the pressure, and ν_T is the kinematic eddy viscosity.

The turbulence closure is given by a k-$\in$ model which, subjected to boundary layer approximation (Rodi 1993), including near-bed damping of turbulence due to sediment concentration (Ruessink et al. 2009), yields ;

$$\frac{\partial k}{\partial t}+u\frac{\partial k}{\partial x}+v\frac{\partial k}{\partial y}+w\frac{\partial k}{\partial z}=\frac{\partial}{\partial z}\left(\frac{\nu_T}{\sigma_k}\frac{\partial k}{\partial z}\right)+\nu_T\left(\left(\frac{\partial u}{\partial z}\right)^2+\left(\frac{\partial v}{\partial z}\right)^2\right)-\in-B \quad (44)$$

$$\frac{\partial \in}{\partial t}+u\frac{\partial \in}{\partial x}+v\frac{\partial \in}{\partial y}+w\frac{\partial \in}{\partial z}=\frac{\partial}{\partial z}\left(\frac{\nu_T}{\sigma_\in}\frac{\partial \in}{\partial z}\right)+C_{\in 1}\frac{\in}{k}\nu_T\left(\left(\frac{\partial u}{\partial z}\right)^2+\left(\frac{\partial v}{\partial z}\right)^2\right)-C_{\in 2}\frac{\in^2}{k}-C_{\in 3}\frac{\in}{k}B \quad (55)$$

where k is the turbulent kinetic energy, $\in$ is the turbulent dissipation rate, and $B=N^2\nu_T/\sigma_p$ is the buoyancy flux. The Brunt-Vaisala frequency N is $\sqrt{-g/\rho_t\frac{\partial \rho_t}{\partial z}}$, where g is the acceleration due to gravity and $\rho_t=s\rho c+\rho(1-c)$ is the fluid-sediment density (s is the specific gravity of the sediment and c is the sediment concentration) adopted from Fuhrman et al. (2013). Usually, ρ_t approaches ρ as the distance from the bed increases and sediment concentration decreases (also stated as turbulence damping). Inclusion of the buoyancy flux B in

the $k-\in$ equations, while not standard practice, can be important for flows with high suspended sediment concentrations near the bed, especially for sheet flow of fine sands. The current approach to include the damping of turbulence by sediments is taken from Ruessink et al. (2009). The purpose of buoyancy term in the TKE equations is to dampen the turbulence in the close vicinity of the seabed due to the high sediment concentration. In the present case the velocity is only affected in the close vicinity of the seabed where the velocity is approaching zero at $z=z_0$ and thus this approach yields the necessary damping of the near-bed velocity, as previously applied by Ruessink et al. (2009), and later by Fuhrman et al. (2013). This has also been demonstrated by Conley et al. (2008) and Kranenburg et al. (2013), who showed pictures on the effect of the turbulence damping on the current profiles.

The turbulent viscosity is given by

$$\nu_T = c_1 \frac{k^2}{\in} \qquad (66)$$

MERGEFORMAT ()

The standard values of the model constants have been adopted, i.e. $(c_1, c_{\in 1}, c_{\in 2}, \sigma_k, \sigma_\in, \sigma_p) = (0.09,\ 1.44,\ 1.92,\ 1.00,\ 1.30,\ 0.7)$ Rodi (1993). Here, $c_{e3}=1$ for $N^2<0$ and $c_{e3}=0$ for $N^2>0$ (Burchard 2002).

The instantaneous dimensionless bedload transport Φ is given by Nielsen (1992) as a function of the Shields parameter Θ.

$$\Phi = 12\Theta^{\frac{1}{2}}(\Theta - \Theta_c)\frac{\Theta}{|\Theta_c|} \qquad (77)$$

MERGEFORMAT ()

where

$$\Phi = \frac{q_b}{\left[g(s-1)d_{50}^3\right]^{\frac{1}{2}}} \qquad (88)$$

MERGEFORMAT ()

$$\Theta = \frac{\tau_b}{\rho g(s-1)d_{50}} \qquad (99)$$

MERGEFORMAT ()

Here the instantaneous dimensional bedload transport is represented by q_b, the dimensional instantaneous sea bed shear stress by τ_b , the density ratio between the bottom sediments and the water by $s = 2.65$ taken as for quartz sand, and the median grain size diameter by d_{50}. It is important to mention that equation by Nielsen (1992) gives best predictions for the sediment grain sizes considered in the present study. Bedload transport takes place when the critical Shields parameter $\Theta_c = 0.05$ (Dey 1999) is exceeded.

The suspended sediment concentration c is given by:

$$\frac{\partial c}{\partial t} + u\frac{\partial c}{\partial x} + v\frac{\partial c}{\partial y} + w\frac{\partial c}{\partial z} = \frac{\partial (w_s c)}{\partial z} + \frac{\partial}{\partial z}\left(\in_s \frac{\partial c}{\partial z}\right) \qquad (10)$$

MERGEFORMAT ()

$$\in_s = \nu_T + \nu \qquad (11)$$

MERGEFORMAT ()

Eq. (10) has been obtained using the boundary layer approximation. Here, w_s is the settling velocity of sediments, $\in_s$ is the diffusivity of the sediment, and ν is the kinematic viscosity of water. The sediment settling velocity is specified as in van Rijn (1993) with the correction for hindered sediment settling given by Richardson and Zaki (1954), i.e. given as $w_s = w_s^*(1 - c^*)^n$. Here, w_s^* is the settling velocity of sediments in clear water, c^* is the volumetric concentration of the sediments and n is an empirical parameter depending upon the median grain diameter. For median grain diameters considered in this work $n = 4$ (van Rijn 1993) is applied.

Simplification of equations

The permanent wave form approximation is applied to simplify Eqs. (1-5) and Eq. (10). For a flow quantity ϕ beneath linear and a second order Stokes wave, the permanent wave form simplification is given as

$$\frac{\partial \phi}{\partial x} = -\frac{\cos\theta}{c_p}\frac{\partial \phi}{\partial t} \qquad (12)$$

MERGEFORMAT ()

$$\frac{\partial \phi}{\partial y} = - \frac{\sin\theta}{c_p} \frac{\partial \phi}{\partial t}$$ (13)

here $c_p = \omega / k_p$ is the wave celerity, where $k_p = 2\pi/\lambda$ is the wave number in the direction of wave propagation, θ is the angle between the waves and the free stream current (see Fig. 1), ω is the wave frequency and λ is wave length. This simplification reduces the three-dimensional boundary layer equations to spatially one-dimensional equations. By using the continuity equation (Eq. 3) and applying the permanent wave form simplification, the vertical velocity component is given as

$$w = - \int_{z=z_0}^{z} \frac{\partial u}{\partial x} dz - \int_{z=z_0}^{z} \frac{\partial v}{\partial y} dz = \frac{\cos\theta}{c_p} \int_{z=z_0}^{z} \frac{\partial u}{\partial t} dz + \frac{\sin\theta}{c_p} \int_{z=z_0}^{z} \frac{\partial v}{\partial t} dz$$ (14)

MERGEFORMAT ()

Here $w = 0$ at $z = z_0$

Boundary conditions

A no-slip condition is applied at the bed under the assumption of hydraulically rough sea bed.

$$u = 0, v = 0, w = 0, \text{ at } z = z_0$$ (15)

MERGEFORMAT ()

The boundary conditions for k and $\in$ are given in a standard manner (Rodi 1993) using a logarithmic velocity profile as shown in Eqs. (18 and 19), where U_* is friction velocity which is calculated using the rough wall log-law following (Dey 2014).

$$k = \frac{\nu_T \left[\left(\frac{\partial u}{\partial z} \right)^2 + \left(\frac{\partial v}{\partial z} \right)^2 \right]^{\frac{1}{2}}}{\sqrt{c_1}}$$ (16)

MERGEFORMAT ()

$$\in = (c_1)^{\frac{3}{4}} \frac{k^{\frac{3}{2}}}{k z_0}$$ (17)

MERGEFORMAT ()

$$\nu_T \left[\left(\frac{\partial u}{\partial z} \right)^2 + \left(\frac{\partial v}{\partial z} \right)^2 \right]^{\frac{1}{2}} = U_*^2 \quad (18)$$

$$U_* = \frac{\left(k\sqrt{u_1^2 + v_1^2} \right)}{\ln\left(z_1 / z_0 \right)} \quad (19)$$

Here $k = 0.4$ is the von Karman constant, and (u_1, v_1) are the horizontal velocity components at the grid point z_1 nearest the bed.

The reference sediment concentration c_a is obtained using the Zyserman and Fredsøe (1994) formula:

$$c_a = \frac{0.331(\Theta - \Theta_c)^{1.75}}{1 + 0.720(\Theta - \Theta_c)^{1.75}} \quad \text{at } z = z_a = 2d_{50} \quad (20)$$

At the upper boundary, located at $z = z_{\max}$, the velocity is given as:

$$u = U_\infty \cos\theta + U_c \quad (21)$$

$$v = U_\infty \sin\theta \quad (22)$$

Where U_∞ is the horizontal near-bed wave velocity component as defined in Eq. (23-24) (see Afzal et al. (2015; Fig. 1), U_c is the mean current velocity and θ is the angle of attack of the waves on the current at $z_{\max}$ which is equivalent to driving the current with an upper lid. This hydrodynamic model was validated (see Afzal et al. (2015; Fig. 7)) against measurements by Yuan and Madsen (2015) conducted in an oscillating water tunnel with combined horizontally uniform second order Stokes forcing and current. The sensitivity of the location of $z_{\max}$ was also investigated by Afzal et al. (2015; Fig. 6).

213 The velocities (U_∞, W_∞) are obtained from second order Stokes theory (Dean and Dalrymple
2141991).

$$U_\infty(x,y,z,t) = \pm a\frac{gk_p}{\omega}\frac{\cosh(k_p z)}{\cosh(k_p h)}\cos(k_p x\cos\theta + k_p y\sin\theta - \omega t)$$
$$\pm\frac{3}{4}\frac{a^2\omega k_p\cosh(2k_p z)}{\sinh^4(k_p h)}\cos 2(k_p x\cos\theta + k_p y\sin\theta - \omega t)$$

215 (23)

$$W_\infty(x,y,z,t) = \pm a\frac{gk_p}{\omega}\frac{\sinh(k_p z)}{\cosh(k_p h)}\sin(k_p x\cos\theta + k_p y\sin\theta - \omega t)$$
$$\pm\frac{3}{4}\frac{a^2\omega k_p\sinh(2k_p z)}{\sinh^4(k_p h)}\sin 2(k_p x\cos\theta + k_p y\sin\theta - \omega t)$$

216

217 where the upper sign is used for waves following the current whereas the lower sign is used
218for waves opposing the current. The near-bottom velocities are obtained from evaluating these
219free stream velocities at $z = z_{\max}$. Here a is the free surface linear wave amplitude.

220 Since the velocity at $z = z_{\max}$ is taken as the free stream velocity, zero flux conditions for the
221turbulent quantities k and $\in$ are imposed as

$$\frac{\partial k}{\partial z} = 0$$

222 (24)

$$\frac{\partial \in}{\partial z} = 0$$

223 (25)

224 The sediment concentration at $z = z_{\max}$ is obtained using a zero flux condition (Eq. 26)

$$\nu_T\frac{\partial c}{\partial z} + w_s c = 0$$

225 (26)

Following Fredsøe et al. (1985), Eq. (26) can be approximated by vanishing sediment concentration at $z = z_{max}$, due to the rapid decay of the suspended sediment concentration with the distance from the bed.

$$c \to 0 \text{ when } z \to \infty \tag{27}$$

Forcing function

Due to the boundary layer approximation the horizontal pressure gradient is constant through the boundary layer and is obtained from the near-bottom free stream (potential flow) velocity field (U_∞, W_∞).

$$-\frac{1}{\rho}\frac{\partial p}{\partial x} = \frac{\partial U_0}{\partial t} + U_0\frac{\partial U_0}{\partial x} + V_0\frac{\partial U_o}{\partial y} - \frac{1}{\rho}\frac{\partial p_c}{\partial x} \tag{28}$$

$$-\frac{1}{\rho}\frac{\partial p}{\partial y} = \frac{\partial V_0}{\partial t} + U_0\frac{\partial V_0}{\partial x} + V_0\frac{\partial V_o}{\partial y} - \frac{1}{\rho}\frac{\partial p_c}{\partial y} \tag{29}$$

where

$$U_0 = U_\infty \cos\theta,\ V_0 = U_\infty \sin\theta,\ W_0 = W_\infty \tag{30}$$

where U_∞ is the velocity component in the wave propagation direction and W_∞ is the corresponding vertical velocity component, and where $\partial p_c/\partial x$ and $\partial p_c/\partial y$ represent the constant pressure gradient in x- and y-direction, respectively, due to the current. Previous calculations by e.g. Davies and Li (1997) and Holmedal and Myrhaug (2009) show that the term $W_0\frac{\partial U_0}{\partial z}$ (and thus $W_0\frac{\partial V_0}{\partial z}$ at the upper boundary is about three order of magnitudes smaller than the other convective terms, and hence $W_0\frac{\partial U_0}{\partial z}$ and $W_0\frac{\partial V_0}{\partial z}$ have been neglected in Eqs. (28 and 29).

Numerical method and initial conditions

Eqs. (1), (2), (4), (5) and (10) are solved using a finite difference method (second order central differences) in space with geometric stretching near the bed. A staggered vertical grid arrangement is used to store the turbulent quantities k and $\in$ at the boundaries of the velocity u cells. Here 100 grid points with a geometric stretching factor of 1.09 is applied; previous experience show that this grid resolution is sufficient to obtain grid independent results, and to predict the seabed shear stress correctly (see e.g. Holmedal et al. (2003; Fig 5)). By using a second order central finite difference discretization in the vertical direction and using the permanent wave form approximation given in Eqs. (12-14), the governing Eqs. (1-5) and Eq. (10) are reduced to a set of nonlinear, coupled ordinary differential equations which are integrated in time with the appropriate boundary conditions given in Eqs. (15-27). This discretization is given by Afzal et al. (2015; Appendix A) for the hydrodynamic equations. Here a staggered grid was employed such that k and $\in$ are evaluated at the boundaries of (u,v) cells. Furthermore, the grid for the sediment concentration is a subset of the grid for the velocities, since the near-bed boundary condition for c is given at a fixed elevation above the rough bottom. The integration in time is obtained using the integrator VODE (Brown et al. 1989). Small positive values of the mean turbulence and flow quantities were initially seeded, and the equations were integrated in time until the flow was fully developed. In order to establish a fully developed flow (in the sense that wave-averaged quantities remain the same after successive wave periods), a spin-up time of 800 wave periods was applied. An extra simulation of 6400 wave periods was done for all the cases to make sure that the spin-up time of 800 wave period is sufficient. Here 100 vertical grid cells were found to be sufficient for resolving the boundary layer.

Comparison with experiments

The model has been validated against both oscillatory water tunnel experiments (Dohmen-Janssen et al. 2001) and wave flume experiments (Dohmen-Janssen and Hanes 2002). Here, the oscillatory water tunnel experiments were conducted with symmetric forcing plus a mean current (and thus no streaming effects are present) while the wave flume measurements (second-order

Stokes progressive waves) contain both Longuet-Higgins streaming and streaming due to wave skewness.

Dohmen-Janssen et al. (2001) published measurements of the sediment concentration profiles for sheet flow conditions over a sand bed. Experiments were carried out in the Large Oscillating Water Tunnel (LOWT) of Delft Hydraulics (now Deltares) where oscillatory flow plus a net current were simulated at large scale. The test section was 12 m long, 0.3 m wide and the water depth was 0.8 m in these measurements. A re-circulation system allowed generation of a net current in addition to the oscillatory flow (excursion amplitude 1.47 m). An oscillation period of T = 7.2 s was chosen. These experiments were carried out with three median grain sand size diameter (d_{50} =0.13, 0.21 and 0.32 mm) and with mean currents of 0.24, 0.23 and 0.26 m/s respectively.

Figure 2 shows the predicted and measured wave-averaged suspended sediment concentration profile $\overline{c(z)}$ for the experimental data from Dohmen-Janssen et al. (2001; Fig. 10). Here different settling velocities w_s have been applied to investigate the behaviour of the present model. The predicted mean suspended sediment concentration $\overline{c(z)}$ obtained by applying the measured settling velocities given by Dohmen-Janssen et al. (2001) and the settling velocities obtained by the Soulsby (1997) formula are in good agreement with the measurements obtained for medium sand (d_{50} = 0.21 mm) and for fine sand (d_{50} = 0.13 mm) while for coarse sand (d_{50} =0.32 mm) $\overline{c(z)}$ is under predicted . These predictions are in qualitative agreement with those obtained by Dohmen-Janssen et al. (2001) from their 1-D sediment-diffusion model using the still water settling velocity w_s = 0.0119 m/s for d_{50} = 0.13 mm, w_s = 0.0260 m/s for d_{50} = 0.21 mm, and w_s = 0.0429 m/s for d_{50} = 0.32 mm. Also, Malarkey et al. (2003) and Holmedal et al. (2004) obtained similar predictions using 1-D sediment-diffusion models. **The inclusion of turbulence suppression and hindered settling terms in the present model works best for flows with high suspended sediment concentration (fine and medium grains) as discussed by Dohmen-Janssen et al. (2001) and Fuhrman et al. (2013). For coarse sand (e.g. d_{50} = 0.32 mm), it**

appears that decreasing the settling velocity w_s from 0.0429 m/s to 0.030 m/s for d_{50} = 0.32 mm leads to the mean suspended sediment profile being well predicted by the present model. The reason for this is unclear to the authors, but as discussed previously, the settling velocity is introduced to model the effect of the gravity on the sediment particles; it is not obvious that this is always well modelled by using the still water value of w_s. The uncertainty in the estimation of hydrodynamic lift and different components of hydrodynamic lift in modeling the entrainment threshold of sediments has also recently been discussed by Dey et al. (2020).

Dohmen-Janssen and Hanes (2002) published measurements of sediment concentration and wave-averaged sediment transport under surface gravity waves in a large-scale wave flume using natural sand with a median grain diameter d_{50} = 0.24 mm. The flume is 300 m long, 5 m wide and the water depth was 3.5 m in these measurements. Here the wave-averaged sediment transport was measured from four different combinations of wave heights and wave periods. For test case *mi* (H_{des} = 1.35 m, T = 6.5 s, $\overline{q_s}$ = 33.8 m^2/s, σ_{qs} = 16.4 m^2/s), $\overline{q_{sp}}$ was calculated to be 28.9 m^2/s. Here H_{des} is the design wave height at the wave maker, $\overline{q_s}$ and $\overline{q_{sp}}$ are the measured and predicted wave-averaged sediment transport, respectively, and σ_{qs} is the standard deviation of q_s. Corresponding values of $\overline{q_{sp}}$ for other tests *mh* (H_{des} = 1.6 m, T = 6.5 s, $\overline{q_s}$ = 42.9 m^2/s, σ_{qs} = 15.6 m^2/s), *mf* (H_{des} = 1.3 m, T = 9.1 s, $\overline{q_s}$ = 76.7 m^2/s, σ_{qs} = 6.4 m^2/s) and *mc* (H_{des} = 1.5 m, T = 9.1 s, $\overline{q_s}$ = 107.3 m^2/s, σ_{qs} = 17.7 m^2/s) was found to be 49.5, 62.6 and 117.1 m^2/s, respectively. Similar to Gonzalez-Rodriguez and Madsen (2011) and Kranenburg et al. (2012), the wave-averaged sediment transport from Dohmen-Janssen and Hanes (2002) is predicted by the mean bedload transport $\overline{q}_{bt}$. Here, the predictions have been obtained using second order Stokes waves to drive the sea bed boundary layer. Overall, it appears that the predictions are in excellent agreement with the measurements; $\overline{q_{sp}}$ lies well within $\overline{q_s} \pm 2\sigma_{qs}$ for

three of the measurements, while for the other measurement (mf) it lies slightly outside this interval.

Figure 3 shows the predicted and measured wave-averaged suspended sediment concentration profile $\overline{c(z)}$ for the test condition mh i.e. T = 6.5 s and H_{des} = 1.6 m where H_{des} is the design wave height at the wave maker. The settling velocities w_s = 0.027 m/s and w_s = 0.028 m/s, obtained from Dohmen-Janssen et al. (2001) and Soulsby (1997), respectively, have been applied in the present model; here the settling velocity w_s = 0.027 m/s is obtained by interpolating the settling velocities w_s = 0.030 m/s for d_{50} = 0.32 mm and w_s = 0.026 for d_{50} = 0.21 mm which gave the best predictions of the oscillating water tunnel measurements by Dohmen-Janssen et al. (2001) as shown in Fig. 2. The present model yields slightly better predictions when using these settling velocities than when using the settling velocity taken from Soulsby (1997). In both simulations, the predicted mean suspended sediment concentration is in fair agreement with the measurements near the bed (for $z < 30$ mm) while the predictions are poorer farther up in the water column (for $z > 30$ mm). However, Dohmen-Janssen and Hanes (2002) themselves stated that the relatively small vertical gradient in the measured suspended sediment concentrations above 3 cm is ‘perplexing’; they suggested that this might be caused by a build-up of background turbulent kinetic energy and/or an accumulation of fine sediments above the boundary layer. The results obtained from the present one-phase sediment diffusion model is also compared with those obtained by Hsu and Liu (2004) and Ma et al. (2014) (both using two-phase models) who also compared their numerical simulations against the experimental data from Dohmen-Janssen and Hanes (2002, Fig. 6). As clearly shown in Fig. 3, the two-phase models yield similar predictions of the measurements as the present one-phase model for this data set, thus supporting Dohmen-Janssen and Hanes (2002) own assumption of non-ideal conditions in the experiments leading to surprisingly high values of $\overline{c(z)}$ for $z > 30$ mm.

RESULTS AND DISCUSSION

The sediment transport due to streaming and wave-current interaction in the turbulent bottom boundary layer is investigated for realistic wave and current conditions. Here the amplitude of

ocean surface waves is a =1.22 m and the wave period is 6 s. These waves propagate over a flat rough bottom. Here, the current U_c =0.1 m/s is specified at $z_{\max}$ =0.25 m above the bottom (U_c is fixed in the x-direction). The angle θ representing the direction of waves propagation relative to current varies from 0° to 180°; the water depth is 8 m and the wave length is 45 m. Furthermore, the median sand grain diameter is d_{50} = 0.21 mm corresponding to A/k_N = 1800 where A is the near-bottom wave excursion amplitude and k_N =2.5, d_{50}. The corresponding settling velocity is w_s = 0.026 m/s, taken from Dohmen-Janssen et al. (2001). These wave conditions represent intermediate water depth ($k_p h = 1.11$) with wave steepness $ak_p = 0.17$. Overall, it is expected that the obtained results will be qualitatively similar to other wave-dominated wave-current flows. The dispersion relation for waves alone has been applied neglecting the effect of the current. This is a reasonable approximation since the current here is weak compared to the waves as discussed in detail by Holmedal et al. (2013).

Eulerian wave-averaged suspended sediment transport

It is recalled that wave-induced seabed boundary layer streaming over a flat bed with homogeneous roughness is caused by two different mechanisms. The first mechanism can be explained by that, because of friction, the horizontal and vertical velocity components u and w are not 90° out of phase within the seabed boundary layer (as they are outside where there is no friction and potential flow applies). Thus, $\overline{uw}$ (where the bar denotes wave-averaging) is non-zero and varying vertically such that $\frac{\partial \overline{uw}}{\partial z}$ acts as a depth-varying pressure gradient leading to a near-bed wave-induced current (or drift) in the wave propagation direction. This was first explained by Longuet-Higgins (1953) and is denoted Longuet-Higgins streaming in the forthcoming. It should be noted that Longuet-Higgins streaming only occurs beneath propagating waves where the vertical velocity is non-zero; it is absent for horizontally uniform flow. The other mechanism is caused by wave skewness, which exists both for horizontally uniform second order Stokes forcing and for the near-bed forcing induced by second order propagating Stokes

waves. As first demonstrated experimentally by Ribberink and Al-Salem (1995), this streaming mechanism (due to wave skewness) counteracts the Longuet-Higgins streaming. The interaction between the Longuet-Higgins streaming and the wave skewness induced streaming was discussed in detail by Holmedal and Myrhaug (2009) showing that the streaming induced seabed boundary layer velocity is slightly larger beneath linear propagating waves than beneath second order Stokes propagating waves. However, second order Stokes forcing implies a slightly larger crest value and a slightly smaller trough value of the near-bed velocity that drives the seabed boundary layer; corresponding impact on shear stress crest and trough values will be discussed in detail in the section below.

Waves alone

Figure 4 (a) shows the bed shear stress magnitude $\left|\frac{\tau_b}{\rho}\right|$ over a wave period for horizontally uniform (HU) linear forcing, horizontally uniform (HU) Stokes forcing, linear propagating waves, and second order Stokes waves. It is observed that the crest value is largest for second order Stokes waves and smallest for horizontally uniform linear forcing; while the trough is deepest for horizontally uniform linear forcing and most shallow for second order Stokes waves. The difference in the crest and trough values between horizontally uniform Stokes forcing and linear propagating waves, however, is less obvious.

Although this boundary layer flow is a highly non-linear process where superposition of quantities does not apply, it is useful to look at the separate effects of streaming and forcing to explain the different crest and trough values in Fig. 4 (a). For linear propagating waves streaming due to wave skewness is absent, while for second order Stokes waves, the Longuet-Higgins streaming dominates the streaming caused by wave skewness, leading to a positive near-bed current which is slightly smaller than for linear propagating waves (Holmedal and Myrhaug 2009). The streaming also affects the bottom shear stress; integration of the momentum equation over a control box within the boundary layer (as described in detail by Fredsøe and Deigaard (1992; Ch. 2, Eq. 2.96)) yields the relation $\overline{\tau_b} = -\rho\left(\overline{uw}\right)_\infty$ where $\overline{\tau_b}$ is the mean bottom shear

stress (the bar denotes wave-averaging) and the subscript ∞ denotes the edge of the boundary layer where $\overline{uw}$ is non-zero due to the presence of the friction. For linear propagating waves this leads to an increase of the shear stress crest value; thus the bottom shear stress crest value is larger for linear propagating waves than for horizontally uniform linear forcing where streaming is absent. The second order Stokes forcing implies a slightly larger crest value and a slightly smaller trough value of the near-bed velocity than for linear wave forcing. This results in a larger bottom shear stress crest and a smaller bottom shear stress trough for second order Stokes forcing than for linear wave forcing. It appears that this effect dominates the effect of wave skewness which counteracts the effect of the Longuet-Higgins streaming as discussed in detail in Holmedal and Myrhaug (2009). For the same reasons, the crest value of the bottom shear stress beneath horizontally uniform Stokes forcing is larger and the trough value is smaller than for horizontally uniform linear forcing.

Overall, the bottom shear stress beneath second order propagating Stokes waves exhibit an enhanced crest value both due to the non-linear forcing and due to streaming (where the Longuet-Higgins streaming is dominating the streaming caused by the wave skewness), and thus the crest value of the bottom shear stress is largest for this forcing. It appears that the effect of the second order Stokes forcing and the Longuet-Higgins streaming on the bottom shear stress crest value is of the same magnitude; this is observed from Fig. 4(a) by the crest value beneath propagating linear waves (where Longuet-Higgins streaming occur) being approximately equal to that observed for horizontally uniform second order Stokes forcing.

Figure 4 (b) shows the mean suspended sediment flux $\overline{Uc}(z)$ profiles beneath waves alone for HU linear forcing, HU Stokes forcing, beneath linear propagating waves, and beneath second order propagating Stokes waves. The largest mean suspended sediment flux occurs beneath second order Stokes waves followed by linear propagating waves and HU Stokes forcing; the mean flux beneath HU linear forcing is zero due to the symmetric forcing and absence of streaming. Although the temporal variation of the bed shear stress is almost the same for HU Stokes forcing and linear propagating waves over the wave cycle, the mean suspended sediment flux beneath linear propagating waves is much larger than beneath HU Stokes forcing. This is caused by the non-linear interaction between the instantaneous velocity and the suspended

sediment concentration. The quantity X can be decomposed as $X = \overline{X} + \tilde{X}$ where $\overline{X}$ denotes the time averaged component and $\tilde{X}$ denotes the periodic component. By applying this decomposition on U and c, the sediment flux can be decomposed as $\overline{Uc} = \overline{U}\,\overline{c} + \overline{\tilde{U}\tilde{c}}$, where $\overline{U}\,\overline{c}$ represents the suspended sediment flux associated with the time averaged flow, while $\overline{\tilde{U}\tilde{c}}$ represents the suspended sediment flux associated with the periodic part of the flow. Figure 4 (c) shows that $\overline{U}\,\overline{c}$ is negative for HU Stokes forcing while it is positive for linear propagating waves and second order Stokes waves; for HU linear forcing it is zero. Moreover, $\overline{U}\,\overline{c}$ is larger beneath linear propagating waves than beneath second order Stokes waves. This is because linear propagating waves yields a streaming-induced velocity in the direction of wave propagation (Longuet-Higgins streaming), while second order Stokes waves are also subjected to streaming due to wave skewness which is opposing the wave propagation direction; yielding a smaller streaming-induced current than for linear propagating waves as previously discussed by Holmedal and Myrhaug (2009). Figure 4 (d) shows that the contribution from $\overline{\tilde{U}\tilde{c}}$ to the suspended sediment flux is larger than the contribution from $\overline{U}\,\overline{c}$. The reason is that $\overline{\tilde{U}\tilde{c}}$ depends on the instantaneous phase and magnitude of both U and c; the suspended sediment flux cannot be understood by only discussing $\overline{U}$ and $\overline{c}$ separately as discussed previously by Davies and Li (1997), Holmedal and Myrhaug (2006) and Fuhrman et al. (2013). Here $\overline{\tilde{U}\tilde{c}}$ is largest for second order Stokes waves, followed by linear propagating waves and HU Stokes forcing; for HU linear forcing $\overline{\tilde{U}\tilde{c}}$ is zero. Overall, Figs. 4 (c) and (d) yield a better understanding of the process underpinning the mean suspended sediment profiles shown in Fig. 4 (b).

Combined waves and current

Figures 5 (a) - (d) show the bed shear stress magnitude $\left|\frac{\tau_b}{\rho}\right|$ over a wave period for $\theta = 0^\circ, 45^\circ, 90^\circ, 135^\circ$ and 180° for HU linear forcing, HU Stokes forcing, linear propagating

waves, and second order Stokes waves, respectively. The result follows the same trend as those shown in Fig. 4 (a): the largest crest value is found beneath second order Stokes waves while the smallest crest value is found beneath HU Linear forcing. However, due to the current the bed shear stress magnitude is larger beneath the wave crest than beneath the wave trough for following waves and current $\left(0^\circ < \theta < 90^\circ\right)$, while the opposite occurs for opposing waves and current $\left(90^\circ < \theta < 180^\circ\right)$. Fig. 5 also shows that the bed shear stress crest amplitude decreases and the bed shear stress trough amplitude increases as the angle between the waves and the current increases.

Figures 6 (a) - (d) show the Eulerian wave-averaged suspended sediment flux profiles $(\overline{Uc}(z))$ for $\theta = 0^\circ, 45^\circ, 90^\circ, 135^\circ$ and 180° for waves and current with HU linear forcing, HU Stokes forcing, linear propagating waves, and second order Stokes waves, respectively. Here, $U(z,t) = \sqrt{u(z,t)^2 + v(z,t)^2}$ is the magnitude of the velocity vector. As for waves alone (discussed in Section 3.1.1), the wave-averaged flux is obtained by integrating the product of the instantaneous sediment concentration and velocity over a wave period. Fig. 6 shows that the suspended sediment flux decreases as θ increases. This is related to the decrease of both the bed shear stress amplitude (stirring up less sediments, Figs. 5 a- d) and the velocity with increasing angles between the waves and the current. It appears that the largest mean suspended sediment flux is found beneath second order Stokes waves followed by linear waves, HU Stokes forcing, and HU linear forcing. It should be noted that due to a calculation error, Holmedal et al. (2013) reported a larger mean suspended sediment and bedload transport for linear propagating waves than for second order Stokes waves.

Figure 7 (a) shows the magnitude and direction of the wave-averaged suspended sediment transport $\int_{z_o}^{z_{max}} \overline{Uc} dz$. Here, the directions are represented by vectors (solid lines). For comparison, the wave propagation direction is also represented by vectors (dashed lines). Two major conclusions can be drawn regarding the magnitude of the mean suspended sediment transport: i) The mean suspended sediment transport decreases as the angle between the waves and the

current increases (except for $\theta > 90^{\circ}$ for HU linear forcing due to symmetry around 90°), and ii) For a given angle between the waves and the current, $\int_{z_o}^{z_{max}} \overline{Uc} dz$ is largest for second order Stokes waves, followed by linear propagating waves, HU Stokes forcing, and (for $\theta < 90^{\circ}$) smallest for HU linear forcing. For $45^{\circ}, 90^{\circ}$ and 135°, the transport direction is to the right of the wave propagation direction due to the current. The two different streaming mechanisms (Longuet-Higgins and streaming due to wave skewness) lead to an enhanced mean suspended sediment transport in the wave propagation direction (by changing the phase between U and c, as discussed previously for waves alone; see section 3), thus counteracting the rotation of the mean suspended sediment transport vector towards the current direction. Hence $\int_{z_o}^{z_{max}} \overline{Uc} dz$ is least rotated for second order Stokes waves, more rotated for linear propagating waves, even more rotated for HU Stokes forcing, and most rotated for HU linear forcing where streaming is absent.

Eulerian wave-averaged bedload transport

Figure 7 (b) shows the magnitude and direction of the wave-averaged (mean) total bedload transport $\overline{q}_{bt}$. The direction is represented by vectors (solid lines). For comparison, the wave propagation direction is also represented by vectors (dashed lines). It appears that: i) The mean bedload transport decreases as the angle between the waves and the current increases (except for $\theta > 90^{\circ}$ for HU linear forcing due to symmetry around 90°), and ii) For a given angle between the waves and the current, $\overline{q}_{bt}$ is largest for second order Stokes waves, followed by linear propagating waves, HU Stokes forcing, and (for $\theta < 90^{\circ}$) smallest for HU linear forcing. Similar to the suspended sediment transport, the bedload transport direction is to the right of the wave propagation direction due to the current for $45^{\circ}, 90^{\circ}$ and 135°, and $\overline{q}_{bt}$ is least rotated for second order Stokes waves, more rotated for linear propagating waves, even more rotated for HU Stokes forcing, and most rotated for HU linear forcing where streaming is absent. This similar behaviour

of $\int_{z_o}^{z_{max}} \overline{Uc} dz$ and $\overline{q}_{bt}$ is not surprising since both depend strongly on the bottom shear stress through Eqs. (7-9) and Eq. (20).

Some further insights into the bedload transport dynamics can be obtained by visualizing the bedload transport over a wave period. Fig. 8 (a) shows the near-bed particle trajectories of linear propagating waves plus current for 45° and 135° taken at the grid point nearest the bottom. Here the colour depicts the magnitude of the bedload q_{bt} along the particle trajectory. During one wave period the trajectory starts at the origin, marked by A, then proceeds through B and C and ends at D. Figure 8 (a) reveals that both for 45° and 135° the bedload transport is larger in the wave half-cycle where the particle travels in the wave propagation direction (segment B-C) than in the wave half-cycle where the particle travels against the wave propagation direction (segments A-B and C-D). This leads to a net bedload transport in the wave propagation direction. Furthermore, the bedload transport in the wave half-cycle where the particle travels in the wave propagation direction (segment B-C) is larger for 45° (represented by darker red colour) than for 135°, while the bedload transport in the wave half-cycle where the particle travels against the wave propagation direction (segments A-B and C-D) is smaller for 45° (slightly lighter red colour) than for 135°. Thus the wave-averaged sediment transport is larger for 45° than for 135°.

Figure 8 (b) shows the near-bed trajectories (at the grid point nearest the bottom) beneath waves plus current for $\theta = 45^\circ$ for horizontally uniform linear forcing, horizontally uniform Stokes forcing, linear propagating waves and second order Stokes waves. For all these cases the bedload transport is larger in the wave half-cycle where the particle travels in the wave propagation direction (segment B-C) than in the wave half-cycle where the particle travels against the wave propagation direction (segments A-B and C-D), leading to a net bedload transport in the wave propagation direction. It appears that the bedload transport in the wave half-cycle where the particle travels in the wave propagation direction (segment B-C) is largest for second order Stokes waves (darkest colour) and smallest for HU linear forcing (lightest colour). Furthermore, the bedload transport in the wave half-cycle where the particle travels against the wave propagation direction (segments A-B and C-D) is smallest for second order

Stokes waves (lightest colour) and largest for HU linear forcing (darkest colour). The difference in bedload transport beneath linear propagating waves and HU Stokes forcing is less obvious; this difference cannot be seen directly from Fig. 8 (b). It is observed, though, that the near-bed particle trajectories beneath linear propagating and HU Stokes forcing are different, i.e. the particle excursion is smaller for HU Stokes forcing than for linear propagating waves, and it appears that the bedload transport under linear propagating waves is larger than for HU Stokes forcing. Overall, Fig. 8 (b) visualizes some of the bedload transport dynamics leading to the largest bedload transport for second order Stokes waves, followed by linear propagating waves, HU Stokes forcing and HU linear forcing for $\theta = 45^{\circ}$. Similar results and arguments can be given for the other angles between the waves and the current but this is not elaborated further here.

CONCLUSIONS

In the present work numerical simulations have been applied to investigate how wave-induced streaming, non-linear wave forcing, wave-current interaction and sediment grain size affect the seabed boundary layer sediment dynamics and transport over a flat rough bed for wave dominated flows. Here the sediment transport and dynamics beneath both opposing and following waves and current is investigated; this includes flows where the wave propagation form a non-zero angle with the current, thus extending the present knowledge within this field. These simulations have been conducted for fine, medium and coarse sand ~~for which the present model has been validated using measurement data from both an oscillating water tunnel (Dohmen-Janssen et al. 2001) and a large scale flume (Dohmen-Janssen and Hanes 2002)~~.

For those situations investigated in this work, the mean sediment flux and the mean bedload are both directed along the wave propagation for collinear waves and current; this applies both for following (largest net sediment transport) and opposing (smallest net sediment transport) waves and current. Furthermore, ~~it appears that~~ for colinear waves and current, the largest mean sediment flux and bedload are found beneath second order Stokes waves, despite the mean streaming-induced velocity being slightly smaller beneath second order propagating Stokes waves than beneath linear propagating waves (as previously shown by Holmedal and Myrhaug (2009)). For the mean sediment flux this is due to the non-linear interaction between the instantaneous boundary layer velocity and sediment concentration as previously explained by

e.g. Davies and Li (1997) and Fuhrman et al. (2013); for the mean bedload this is due to the non-linear dependency of the bottom shear stress combined with the effect of the critical value of the bottom shear stress that must be exceeded for bedload to take place. For the more general case where the waves and the current are not colinear, the mean sediment transport (i.e. both the suspended sediment and bedload transport) decreases as the angle between the waves and the current increases. For a given angle between the waves and the current, the sediment transport is largest for second order Stokes waves, followed by linear propagating waves, horizontally uniform Stokes forcing, and smallest for horizontally uniform linear forcing. Furthermore, the mean sediment transport direction (for both the suspended sediments and the bedload) is rotated to the right of the wave propagation direction due to the current (which is directed towards the right). This rotation is largest for horizontally uniform linear forcing, followed by horizontally uniform Stokes forcing, linear propagating waves and second order Stokes waves. One of the limitations of the present study is that the numerical model is sensitive to the selection of settling velocity values since the settling velocity is introduced to model the effect of the gravity on the sediment particles; it is not obvious that this is always well modelled by using the still water value of the settling velocity.

The present work yields new insight into the detailed bottom boundary layer sediment dynamics and transport under combined action of non-collinear waves and current which is a realistic situation in oceans and coastal areas. The study done here is relevant to the areas of transport of sediments/mineral at seabed, transport of fishes, larvae and plankton and also chemical compound spilled in the ocean.

Acknowledgements

This work was carried out mainly as a part of the strategical university program ``Air-Sea Interaction and Transport Mechanisms in the Ocean", funded by the Norwegian Research Council.

Data Availability Statement

Some or all data, models, or code generated or used during the study are available in a repository online in accordance with funder data retention policies. The digitized data measurements of Dohmen-Janssen et al. [2001, Fig. 10], Dohmen-Janssen and Hanes [2002, Fig.

5896 and Table 2], whereas digitized numerical simulation data of Ma et al. [2014, Fig 2], and Hsu
590and Liu [2004, Fig 4] and corresponding modelled data can be found online (at
591https://zenodo.org/record/3563232).

592

Notation

The following symbols are used in this paper:

a = free surface linear wave amplitude (L);

A = near-bottom wave excursion amplitude (L);

B = buoyancy flux (–);

c = sediment concentration (ML^{-3});

c_a = reference sediment concentration (ML^{-3});

c_p = wave celerity (LT^{-1});

c^* = volumetric concentration of the sediments (–);

$\overline{c(z)}$ = wave-averaged suspended sediment concentration profile (–);

d = particle average diameter (L);

d_{50} = median sediment size (L);

g = gravitational acceleration (LT^{-2});

H_{des} = design wave height at the wave maker (L);

k = Turbulent kinetic energy (–);

k_N = Nikuradse equivalent sand roughness (L);

k_p = wave number in the direction of wave propagation (-);

n = empirical parameter depending upon the median grain diameter (-);

N = Brunt-Vaisala frequency (T^{-1});

P = pressure intensity ($ML^{-1}T^{-2}$);

q_b = instantaneous dimensional bedload transport (-);

$\overline{q}_{bt}$ = mean bedload transport (-);

615 $\overline{q_s}$ = measured wave-averaged sediment transport (-);

616 $\overline{q_{sp}}$ = predicted wave-averaged sediment transport (-);

617 R = wave skewness (-);

618 s = specific gravity of the sediment (-);

619 t = time (T);

620 T_p = wave period (T);

621 U_c = mean current velocity (LT^{-1});

622 U_* = friction velocity (LT^{-1});

623 U_∞ = horizontal near-bed wave velocity component (LT^{-1});

624 U_{wc} = crest velocity (LT^{-1});

625 U_{wt} = trough velocity (LT^{-1});

626 $\overline{Uc}$ = sediment flux (MT^{-1});

627 $\overline{Uc}(z)$ = mean suspended sediment flux (MT^{-1});

628 $\overline{U}\,\overline{c}$ = suspended sediment flux associated with the time averaged flow (MT^{-1});

629 $\overline{\tilde{U}\tilde{c}}$ = suspended sediment flux associated with the periodic part of the flow (MT^{-1});

630 u_* = shear velocity (LT^{-1});

631 w_s = settling velocity of sediments(LT^{-1});

632 w_s^* = settling velocity of sediments in clear water (LT^{-1});

633 W_∞ = vertical wave velocity component (LT^{-1});

634 X = quantity term (–);

635 $\overline{X}$ = time averaged component (–);

$\tilde{X}$ = periodic component (–);

z = vertical distance (L);

z_0 = zero-velocity level (L);

σ_{qs} = standard deviation of q_s (–);

Z = Rouse number (–);

ϕ = average friction angle (–);

κ = von Kármán constant (–);

ν = kinematic viscosity of water (L^2T^{-1});

ν_T = kinematic eddy viscosity (L^2T^{-1});

ρ_t = fluid-sediment density (ML^{-3});

ρ = mass density of fluid (ML^{-3});

τ_b = instantaneous sea bed shear stress (MLT^{-2});

$\overline{\tau_b}$ = mean bottom shear stress (MLT^{-2});

$\in$ = Turbulent dissipation rate (–);

θ = angle between the waves and the free stream current (–);

ω = wave frequency (T^{-1});

λ = wave length (L);

$\in_s$ = diffusivity of the sediment (L^2T^{-1});

Φ = instantaneous bedload transport (–);

Θ = Shields parameter (–);

Θ_c = critical Shields number (–);

∞ = edge of the boundary layer (–);

References

Afzal, M. S., Holmedal, L. E., and Myrhaug, D. (2015). “Three-dimensional streaming in the seabed boundary layer beneath propagating waves with an angle of attack on the current.” *Journal of Geophysical Research: Oceans*, 120(6), 4370–4391.

Ali, S. Z., and Dey, S. (2016). “Theory of turbulent flow over a wavy boundary.” *Journal of Hydraulic Engineering*, 142(6), 4016006.

Bose, S. K., and Dey, S. (2014). “Gravity waves on turbulent shear flow: Reynolds averaged approach.” *Journal of Hydraulic Engineering*, 140(3), 340–346.

Brown, P. N., Byrne, G. D., and Hindmarsh, A. C. (1989). VODE: A variable-coefficient ODE solver.” *SIAM J. Sci. Stat. Comput.*, 10(5), 1038–1051.

Burchard, H. (2002). *Applied Turbulence Modelling in Marine Waters*. Lecture Notes in Earth Sciences, Springer Berlin Heidelberg.

Conley, D. C., Falchetti, S., Lohmann, I. P., and Brocchini, M. (2008). “The effects of flow stratification by non-cohesive sediment on transport in high-energy wave-driven flows.” *Journal of Fluid Mechanics*, 610, 43–67.

Davies, A. G., and Li, Z. (1997). “Modelling sediment transport beneath regular symmetrical and asymmetrical waves above a plane bed.” *Continental Shelf Research*, 17(5), 555–582.

Dean, R. G., and Dalrymple, R. A. (1991). *Water Wave Mechanics for Engineers and Scientists*. Advanced Series on Ocean Engineering -Volume 2. World Scientific Publishing Company.

Dey, S. (1999). Sediment threshold. Applied Mathematical Modelling, 23, 399–417

Dey, S. (2014). *Fluvial hydrodynamics*. Springer.

Dey, S., Ali, S. Z., and Padhi, E. (2020). “Hydrodynamic Lift on Sediment Particles at Entrainment: Present Status and Its Prospect.” *Journal of Hydraulic Engineering*, 146(6), 3120001.

Dohmen-Janssen, C. M., and Hanes, D. M. (2002). “Sheet flow dynamics under monochromatic nonbreaking waves.” *Journal of Geophysical Research: Oceans*, 107(C10), 13–21.

Dohmen-Janssen, C. M., Hassan, W. N., and Ribberink, J. S. (2001). “Mobile-bed effects in oscillatory sheet flow.” *Journal of Geophysical Research: Oceans*, 106(C11), 27103–

686 27115.

687Fredsøe, J., Anderson, O. H., and Silberg, S. (1985). “Distribution of suspended sediment in
688 large waves.” *J. of Waterway, Port, Coastal end Ocean Eng.*, 111(6), 1041–1059.

689Fuhrman, D. R., Fredsøe, J., and Sumer, B. M. (2009). “Bed slope effects on turbulent wave
690 boundary layers: 2. Comparison with skewness, asymmetry, and other effects.” *Journal of*
691 *Geophysical Research: Oceans*, 114(C3).

692Fuhrman, D. R., Schløer, S., and Sterner, J. (2013). “RANS-based simulation of turbulent wave
693 boundary layer and sheet-flow sediment transport processes.” *Coastal Engineering*, 73,
694 151–166.

695Gonzalez-Rodriguez, D., and Madsen, O. S. (2011). “Boundary-layer hydrodynamics and
696 bedload sediment transport in oscillating water tunnels.” *Journal of Fluid Mechanics*, 667,
697 48–84.

698Holmedal, L. E., Johari, J., and Myrhaug, D. (2013). “The seabed boundary layer beneath waves
699 opposing and following a current.” *Continental Shelf Research*, 65, 27–44.

700Holmedal, L. E., and Myrhaug, D. (2006). “Boundary layer flow and net sediment transport
701 beneath asymmetrical waves.” *Continental Shelf Research*, 26(2), 252–268.

702Holmedal, L. E., and Myrhaug, D. (2009). “Wave-induced steady streaming, mass transport and
703 net sediment transport in rough turbulent ocean bottom boundary layers.” *Continental Shelf*
704 *Research*, 29(7), 911–926.

705Holmedal, L. E., Myrhaug, D., and Eidsvik, K. J. (2004). “Sediment suspension under sheet flow
706 conditions beneath random waves plus current.” *Continental Shelf Research*, 24(17), 2065–
707 2091.

708Holmedal, L. E., Myrhaug, D., and Rue, H. (2003). “The sea bed boundary layer under random
709 waves plus current.” *Continental Shelf Research*, 23(7), 717–750.

710Hsu, T.-J., Jenkins, J. T., and Liu, P. L.-F. (2004). “On two-phase sediment transport: sheet flow
711 of massive particles.” *Proceedings of the Royal Society of London. Series A: Mathematical,*
712 *Physical and Engineering Sciences*, 460, 2223–2250.

713Hsu, T.-J., and Liu, P. L.-F. (2004). “Toward modeling turbulent suspension of sand in the

nearshore.” *Journal of Geophysical Research: Oceans*, 109(C6).

Kranenburg, W. M., Ribberink, J. S., Schretlen, J. J. L. M., and Uittenbogaard, R. E. (2013). “Sand transport beneath waves: The role of progressive wave streaming and other free surface effects.” *Journal of Geophysical Research: Earth Surface*, 118(1), 122–139.

Kranenburg, W. M., Ribberink, J. S., Uittenbogaard, R. E., and Hulscher, S. J. M. H. (2012). “Net currents in the wave bottom boundary layer: On waveshape streaming and progressive wave streaming.” *Journal of Geophysical Research: Earth Surface*, 117(F3).

Lee, S.-K., and Cheung, K. F. (1999). “Laminar and Turbulent Bottom Boundary Layer Induced by Nonlinear Water Waves.” *Journal of Hydraulic Engineering*, 125(6), 631–644.

Longuet-Higgins, M. S. (1953). “Mass Transport in Water Waves.” *Philosophical Transactions of the Royal Society of London. Series A, Mathematical and Physical Sciences*, The Royal Society, 245(903), 535–581.

Ma, G., Chou, Y.-J., and Shi, F. (2014). “A wave-resolving model for nearshore suspended sediment transport.” *Ocean Modelling*, 77, 33–49.

Malarkey, J., Davies, A. G., and Li, Z. (2003). “A simple model of unsteady sheet-flow sediment transport.” *Coastal Engineering*, 48(3), 171–188.

Nielsen, P. (1992). *Coastal bottom boundary layers and sediment transport* (Vol. 4). World scientific.

Nielsen, P., and Callaghan, D. P. (2003). “Shear stress and sediment transport calculations for sheet flow under waves.” *Coastal Engineering*, 47(3), 347–354.

Ribberink, J., Dohmen-Janssen, C., Hanes, D., McLean, S., and Vincent, C. (2000). “Near-Bed Sand Transport Mechanisms under Waves; A Large-Scale Flume Experiment.” *Coastal Engineering 2000*, ASCE, 3263–3276.

Ribberink, J. S., and Al-Salem, A. A. (1995). “Sheet flow and suspension of sand in oscillatory boundary layers.” *Coastal Engineering*, 25(3), 205–225.

Richardson, J. F., and Zaki, W. N. (1954). “Sedimentation and fluidisation: Part I” *Transactions of the Institution of Chemical Engineers*, 32, 35–53.

van Rijn, L. C. (1993). *Principles of sediment transport in rivers, estuaries and coastal seas*

(Vol. 1006, pp. 11-3). Amsterdam: Aqua Publications.

Rodi, W. (1993). Turbulence Models and their Applications in Hydraulics, A State-of-the-art Review. IAHR Monograph Series, 3, *Auflage, AA Balkema, Rotterdam.*

Ruessink, B. G., van den Berg, T. J. J., and van Rijn, L. C. (2009). "Modeling sediment transport beneath skewed asymmetric waves above a plane bed." *Journal of Geophysical Research: Oceans*, 114(C11).

Ruessink, B. G., Michallet, H., Abreu, T., Sancho, F., der A, D. A., der Werf, J. J., and Silva, P. A. (2011). "Observations of velocities, sand concentrations, and fluxes under velocity-asymmetric oscillatory flows." *Journal of Geophysical Research: Oceans*, 116(C3).

Scandura, P. (2007). "Steady streaming in a turbulent oscillating boundary layer." *Journal of Fluid Mechanics*, 571, 265–280.

Schretlen, J., Ribberink, J., and O'Donoghue, T. (2011). "Boundary layer flow and sand transport under full scale surface waves." *Coastal Engineering Proceedings*, 1(32).

Soulsby, R. (1997). *Dynamics of Marine Sands: A Manual for Practical Applications*. Telford.

van der A, D. A., O`Donoghue, T., Davies, A. G., and Ribberink, J. S. (2011). "Experimental study of the turbulent boundary layer in acceleration-skewed oscillatory flow." *Journal of Fluid Mechanics*, 684, 251–283.

Yu, X., Hsu, T.-J., and Hanes, D. M. (2010). "Sediment transport under wave groups: Relative importance between nonlinear waveshape and nonlinear boundary layer streaming." *Journal of Geophysical Research: Oceans*, 115(C2).

Yuan, J., and Madsen, O. S. (2015). "Experimental and theoretical study of wave-current turbulent boundary layers." *Journal of Fluid Mechanics*, 765, 480–523.

Zyserman, J. A., and Fredsøe, J. (1994). "Data analysis of bed concentration of suspended sediment." *Journal of Hydraulic Engineering*, 120(9), 1021–1042.

List of Figures

alone beneath different type of wave forcing; (c) average component $\overline{U}\overline{c}$ of wave-averaged suspended sediment flux in (b); (d) Fluctuating component $\overline{\tilde{U}\tilde{c}}$ of wave-averaged suspended sediment flux in (b). Here HUL refers to horizontally uniform linear waves whereas HUS refers to horizontally uniform Stokes waves.

Mean Eulerian velocity profile for (a) waves following the current and (b) waves opposing the current, sediment concentration profiles for (c) waves following the current and (d) waves opposing the current, suspended sediment flux profiles for (e) waves following the current and (f) waves opposing the current. Here, $A/k_N = 1800$, U_c = 0.1 m/s and $d_{50} = 0.21$ mm for the Dirichlet condition applied at $z_{\max} = 0.25$ cm and 50 cm.

Eulerian wave-averaged suspended sediment flux for different angles between the waves and current ($U_c = 0.1$ m/s) beneath (a) horizontally uniform linear forcing; (b) horizontally uniform Stokes forcing; (c) linear propagating waves; (d) second order Stokes waves.

The (a) wave-averaged suspended sediment transport $\int_{2d_{50}}^{z_{\max}} \overline{Uc}dz$; (b) wave-averaged bedload transport $\overline{q}_{bt}$ beneath different forcing for five different angles θ between the waves and the current.

Near-bed particle trajectories colored on the basis of the magnitude of the bedload transport q_{bt} mm^2/s (a) beneath linear propagating waves and current for $\theta = 45^\circ$ and 135°; (b) with $\theta = 45^\circ$ for different wave forcing.

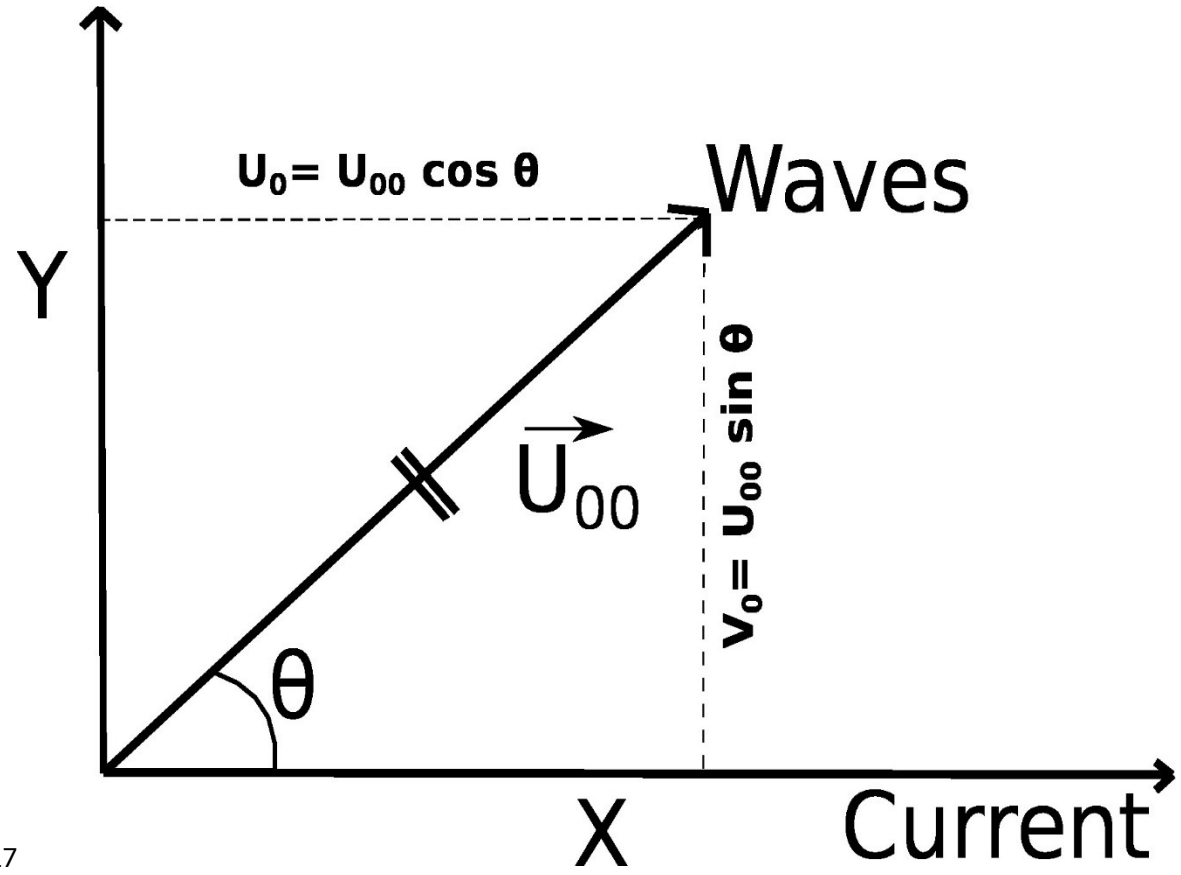

817

818**Fig. 1** Definition sketch

819

820

821

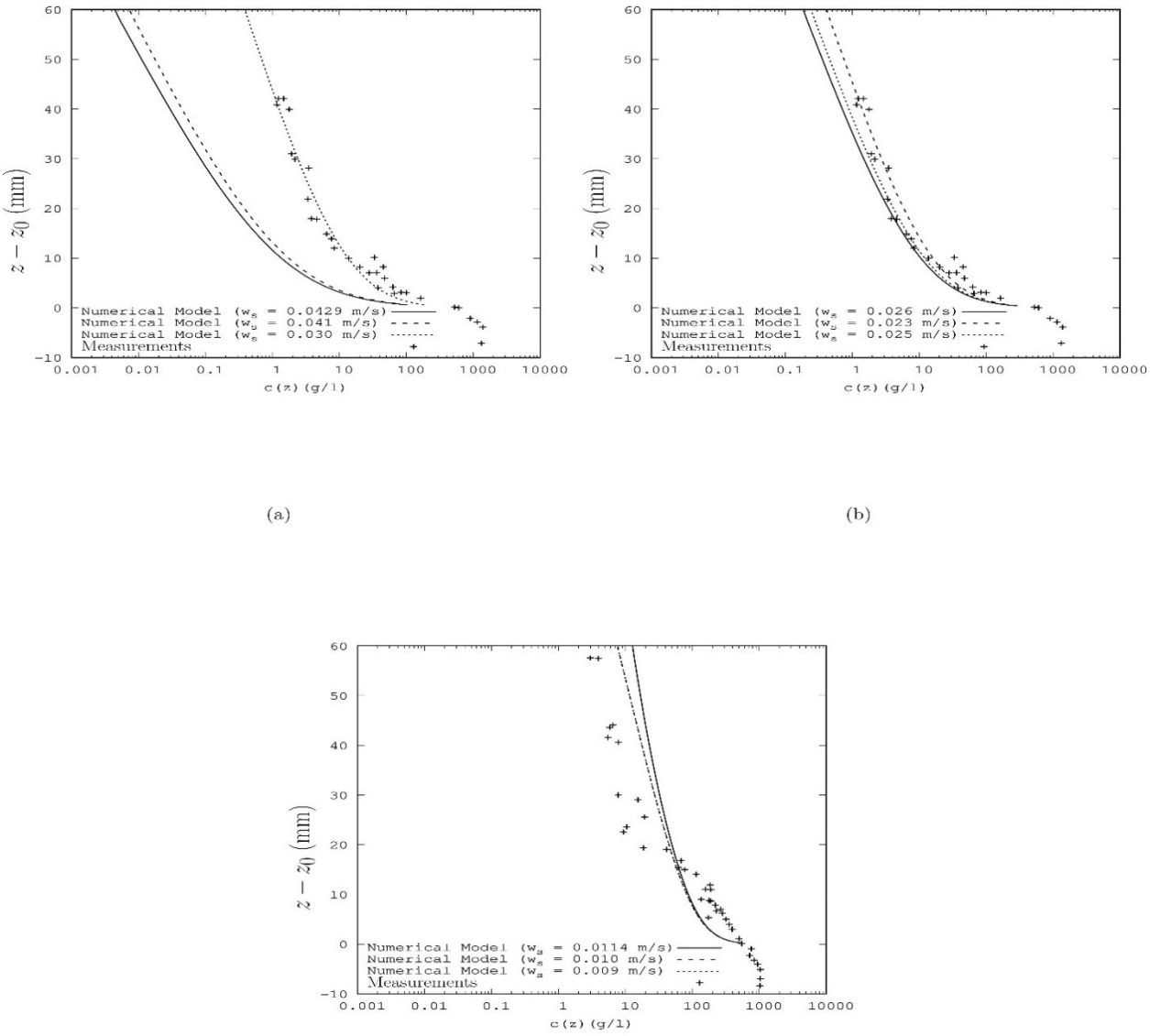

Fig. 2. Magnitudes of the wave-averaged sediment concentration profiles for (a) d_{50} = 0.32 mm, (b) d_{50} = 0.21 mm, (c) d_{50} = 0.13 mm. The plus signs represent experimental data from Dohmen-Janssen et al. (2001) which have been digitized, whereas lines represent simulations. Here, solid line represents numerical simulation with w_s as given by Dohmen-Janssen et al. (2001), dashed line represents numerical simulation with w_s as given by Soulsby (1997), and dotted line

828represents numerical simulation of a calibrated numerical model with w_s as a calibration
829parameter.

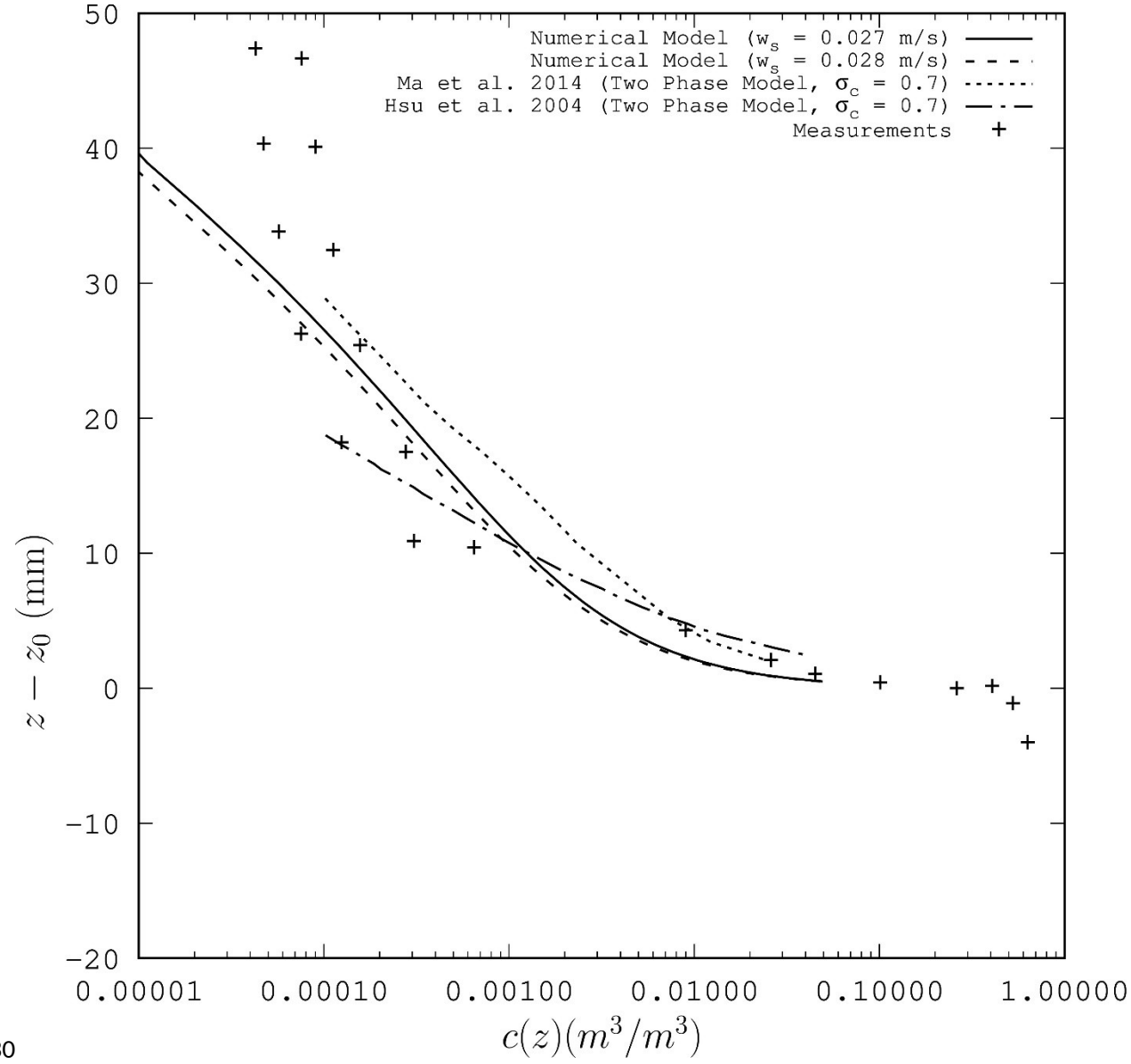

830

831**Fig. 3.** The wave-averaged sediment concentration profile for test mh (T =6.5 s and H_{des} =1.6
832m) in the lower 5 cm above the bed. The plus signs represent experimental data from Dohmen-
833Janssen and Hanes (2002; Fig. 6) which have been digitized, whereas the first two lines (solid
834line and dashed line) show numerical simulations using settling velocities of 0.031 m/s and 0.028
835m/s obtained from Dohmen-Janssen et al. (2001) and Soulsby (1997), respectively. The dotted

836line and the dashed dotted line represents digitized data from Ma et al. (2014) and Hsu and Liu
837(2004), respectively.

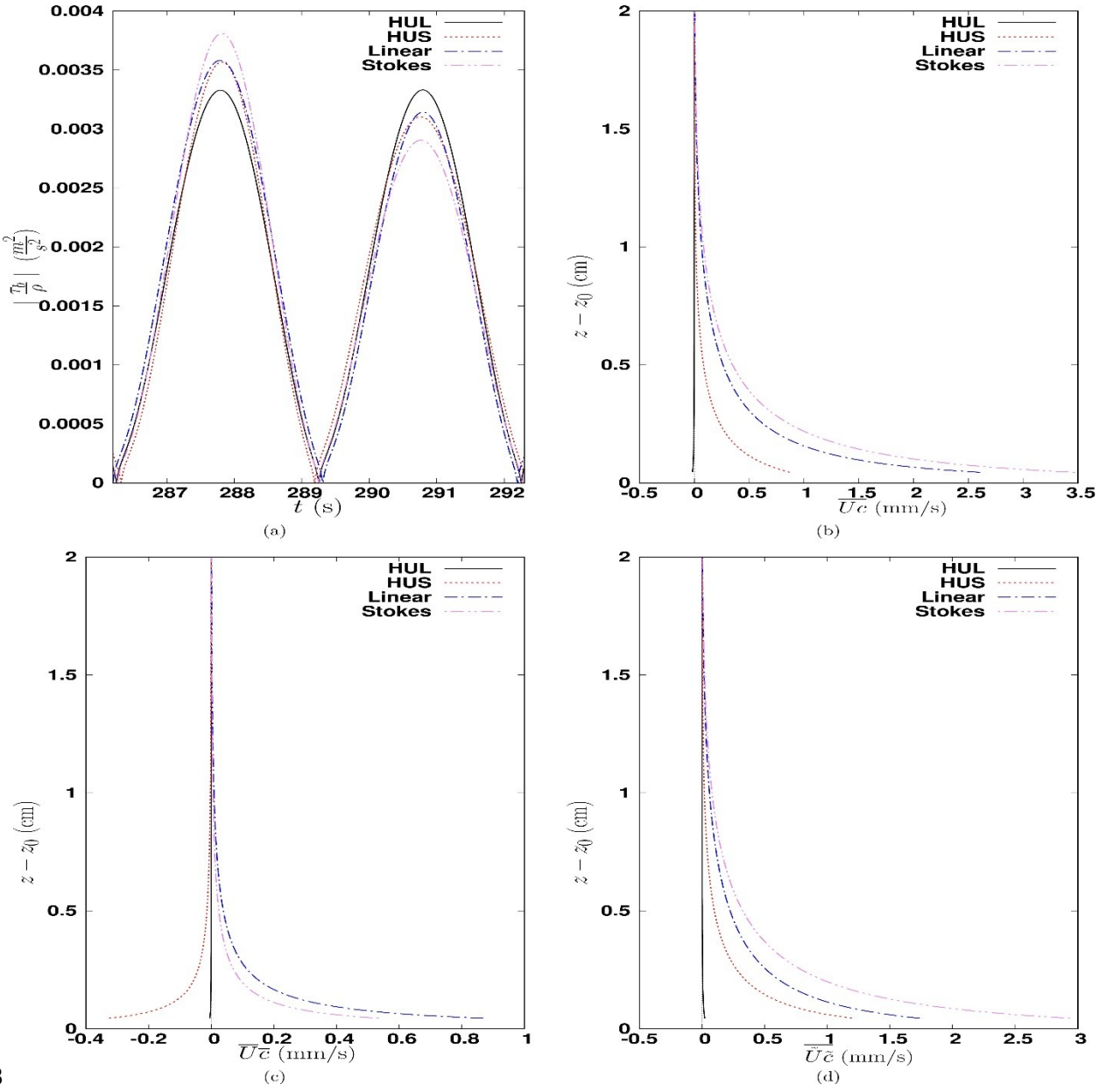

838

839**Fig. 4.** Magnitude of the bed shear stress $\left|\frac{\tau_b}{\rho}\right|$ over a wave period with crest values to the left and
840trough values to the right; (b) Eulerian wave-averaged suspended sediment flux for waves alone
841beneath different type of wave forcing; (c) average component $\overline{Uc}$ of wave-averaged suspended
842sediment flux in (b); (d) Fluctuating component $\overline{\tilde{U}\tilde{c}}$ of wave-averaged suspended sediment flux

843in (b). Here HUL refers to horizontally uniform linear waves whereas HUS refers to horizontally
844uniform Stokes waves.

845

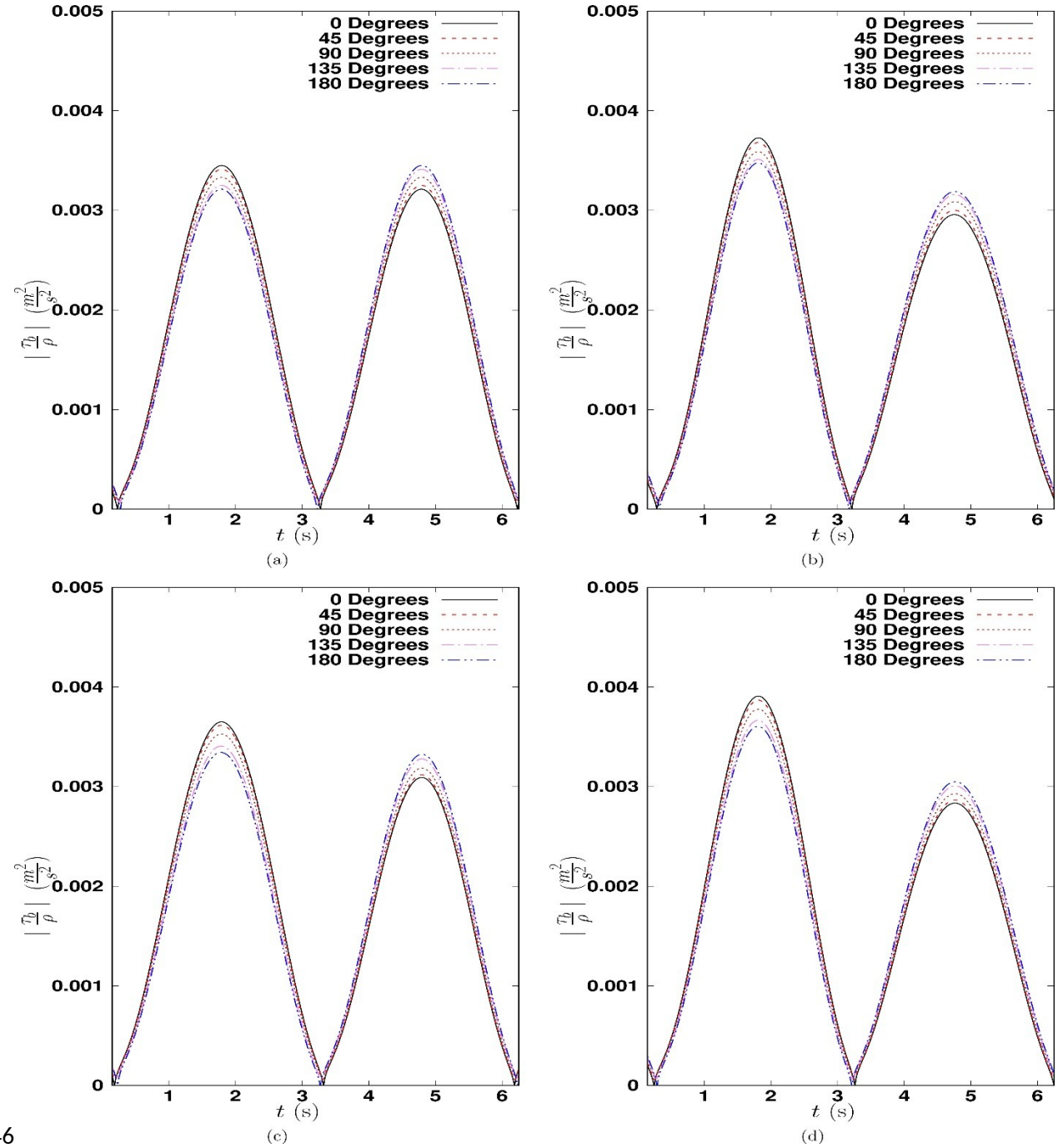

846

Fig. 5. Magnitude of the bed shear stress $\left|\frac{\tau_b}{\rho}\right|$ over a wave period for different angles between the waves and the current beneath (a) horizontally uniform linear forcing; (b) horizontally uniform Stokes forcing; (c) linear propagating waves; (d) second order Stokes waves. Crest values are to the left and trough values are to the right.

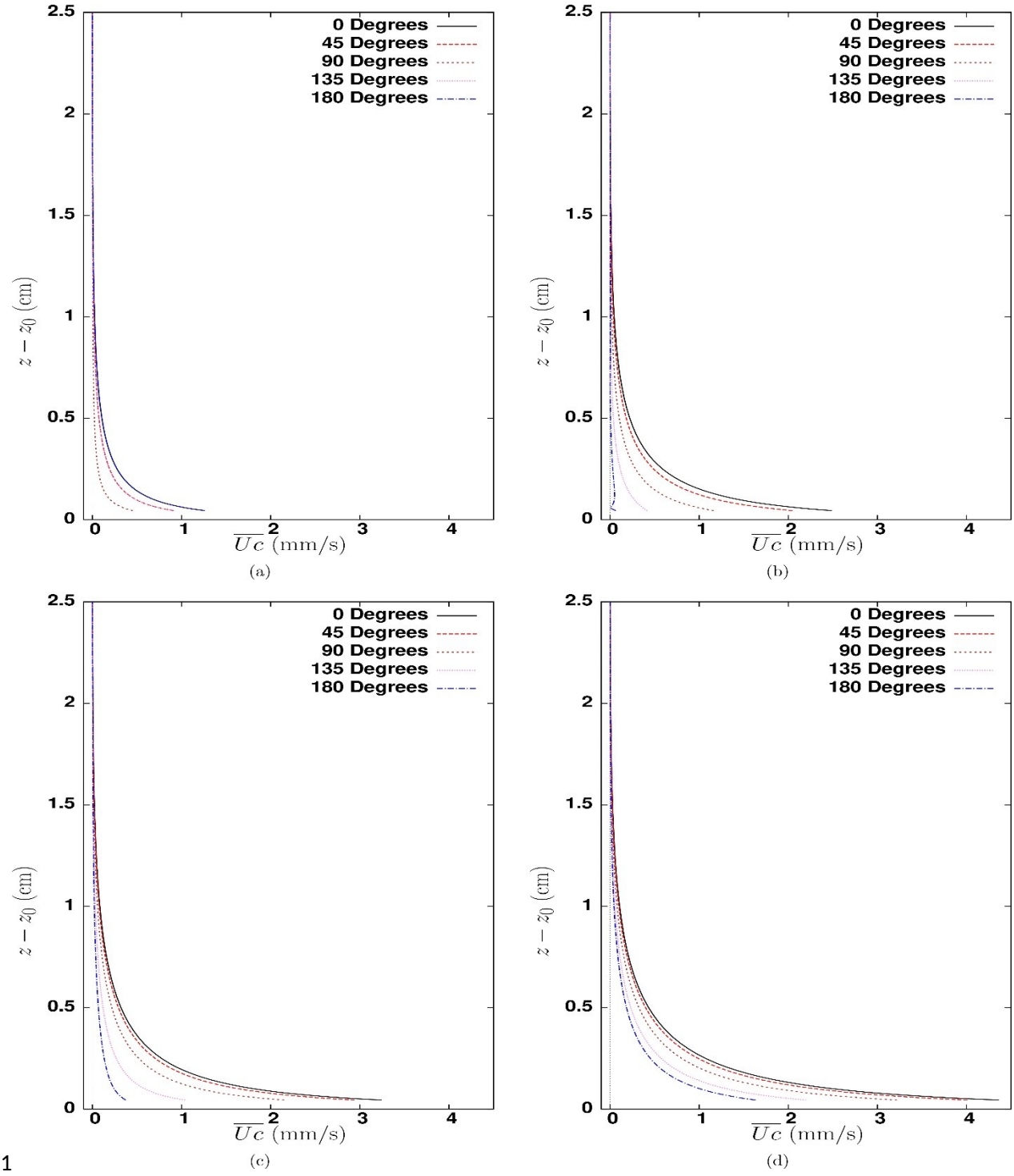

851

852**Fig. 6.** Eulerian wave-averaged suspended sediment flux for different angles between the waves 853and current (U_c =0.1 m/s) beneath (a) horizontally uniform linear forcing; (b) horizontally 854uniform Stokes forcing; (c) linear propagating waves; (d) second order Stokes waves.

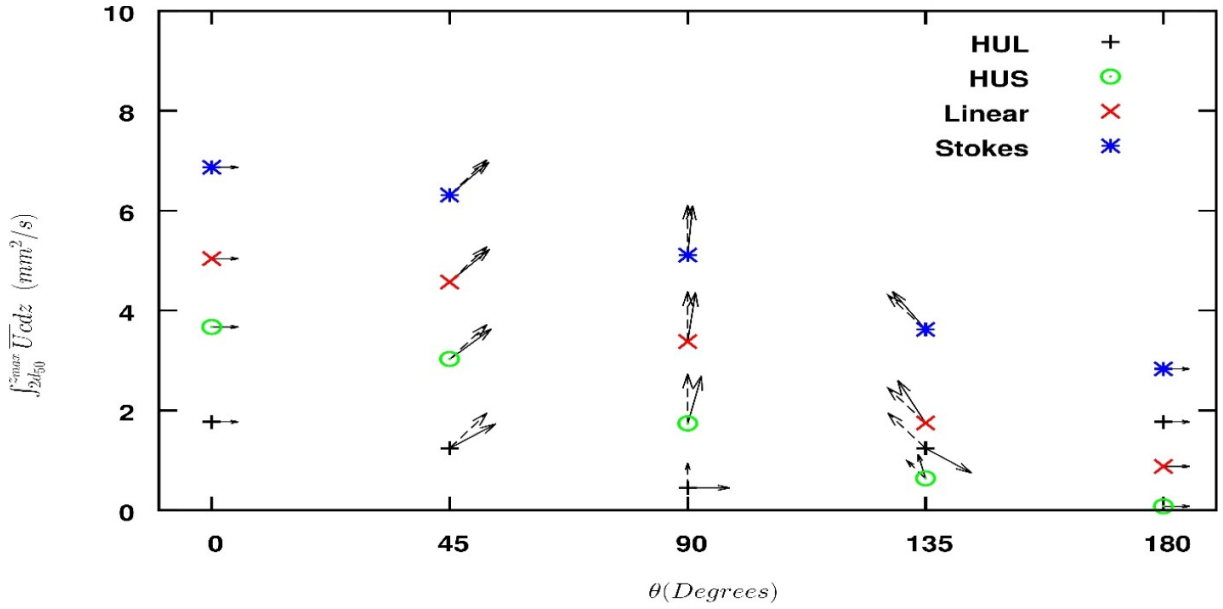

(a)

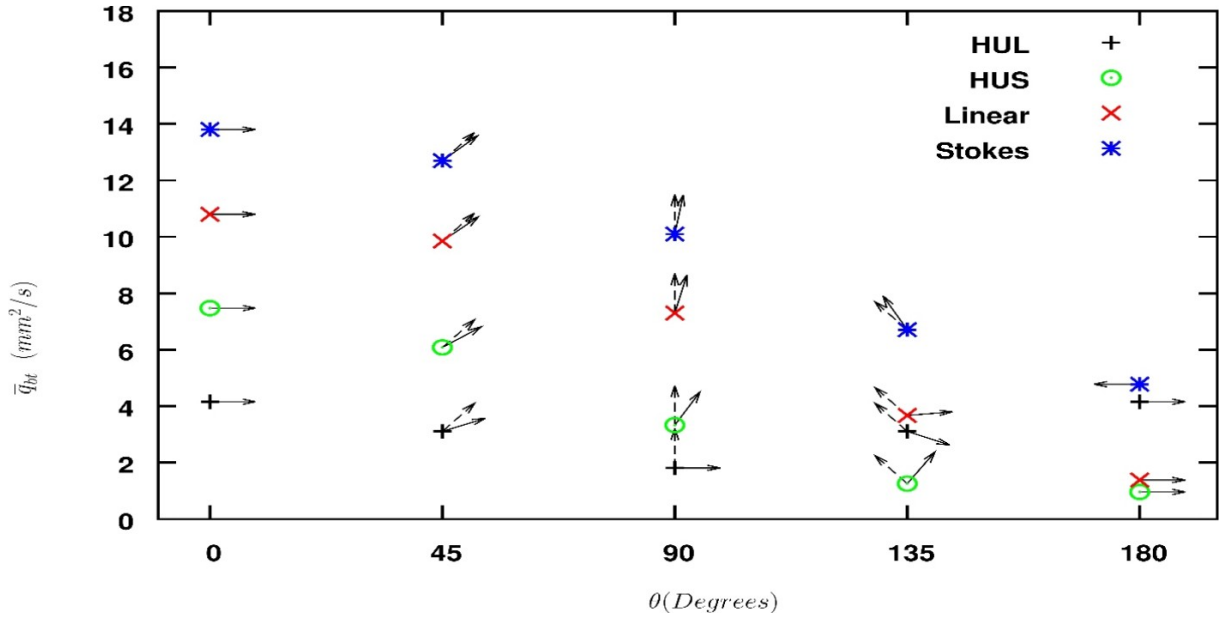

(b)

Fig. 7. The (a) wave-averaged suspended sediment transport $\int_{2d_{50}}^{z_{max}} \overline{U} c dz$; (b) wave-averaged bedload transport $\overline{q}_{bt}$ beneath different forcing for five different angles θ between the waves and the current.

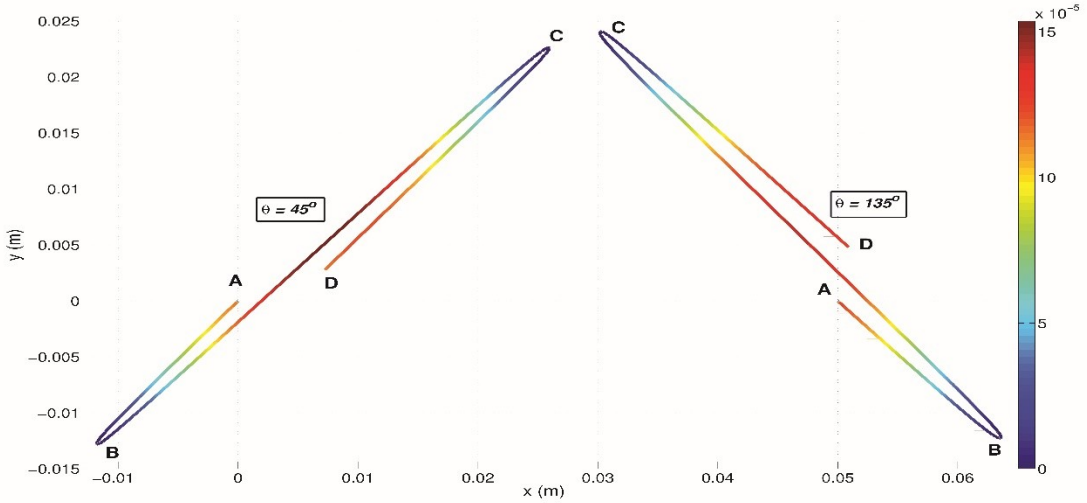

(a)

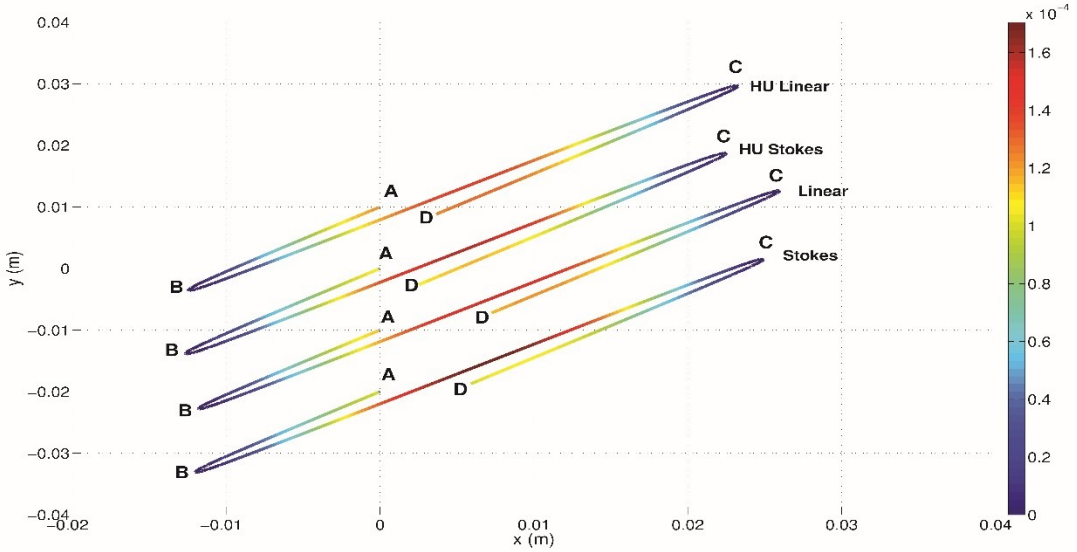

(b)

Fig. 8. Near-bed particle trajectories colored on the basis of the magnitude of the bedload transport q_{bt} mm^2/s (a) beneath linear propagating waves and current for $\theta = 45^\circ$ and 135°; (b) with $\theta = 45^\circ$ for different wave forcing.

872